

Causes and consequences of bimodal grain-size distribution of tephra fall deposited during the August 2006 Tungurahua eruption (Ecuador)

Julia Eychenne · Jean-Luc Le Pennec ·
Liliana Troncoso · Mathieu Gouhier ·
Jean-Marie Nedelec

Received: 11 January 2011 / Accepted: 1 June 2011 / Published online: 30 June 2011
© Springer-Verlag 2011

Abstract The violent August 16–17, 2006 Tungurahua eruption in Ecuador witnessed the emplacement of numerous scoria flows and the deposition of a wide-spread tephra layer west of the volcano. We assess the

Editorial responsibility: R. Cioni

Electronic supplementary material The online version of this article (doi:10.1007/s00445-011-0517-5) contains supplementary material, which is available to authorized users.

J. Eychenne · J.-L. Le Pennec · M. Gouhier
Laboratoire Magmas et Volcans, Clermont Université,
Université Blaise Pascal,
BP 10448, 63000 Clermont-Ferrand, France

J. Eychenne · J.-L. Le Pennec · M. Gouhier
CNRS, UMR 6524, Laboratoire Magmas et Volcans,
5 rue Kessler,
63038 Clermont-Ferrand cedex, France

J. Eychenne (✉) · J.-L. Le Pennec · M. Gouhier
IRD, R 163, Laboratoire Magmas et Volcans,
5 rue Kessler,
63038 Clermont-Ferrand cedex, France
e-mail: J.Eychenne@opgc.univ-bpclermont.fr

L. Troncoso
Instituto Geofísico, Escuela Politécnica Nacional,
Ap. 17-01-2759,
Quito, Ecuador

J.-M. Nedelec
ENSCCF, LMI, Clermont Université,
63177 Aubière, France

J.-M. Nedelec
CNRS, UMR 6002,
63177 Aubière, France

size of the eruption by determining a bulk tephra volume in the range $42\text{--}57 \times 10^6 \text{ m}^3$, which supports a Volcanic Explosivity Index 3 event, consistent with calculated column height of 16–18 km above the vent and making it the strongest eruptive phase since the volcano's magmatic reactivation in 1999. Isopachs west of the volcano are sub-bilobate in shape, while sieve and laser diffraction grain-size analyses of tephra samples reveal strongly bimodal distributions. Based on a new grain-size deconvolution algorithm and extended sampling area, we propose here a mechanism to account for the bimodal grain-size distribution. The deconvolution procedure allows us to identify two particle subpopulations in the deposit with distinct characteristics that indicate dissimilar transport-depositional processes. The log-normal coarse-grained subpopulation is typical of particles transported downwind by the main volcanic plume. The positively skewed, fine-grained subpopulation in the tephra fall layer shares close similarities with the elutriated co-pyroclastic flow ash cloud layers preserved on top of the scoria flow deposits. The area with the higher fine particle content in the tephra layer coincides with the downwind prolongation of the pyroclastic flow deposits. These results indicate that the bimodal distribution of grain size in the Tungurahua fall deposit results from synchronous deposition of lapilli from the main plume and fine ash elutriated from scoria flows emplaced on the western flank of the volcano. Our study also reveals that inappropriate grain-size data processing may produce misleading determination of eruptive type.

Keywords Tephra fall · Bimodal grain size · Volcanic Explosivity Index · Eruption type · Tungurahua volcano

Introduction

Tephra fall deposits are critical in determining the size and type of both modern and ancient explosive eruptions. Current schemes for classifying eruption types (Walker 1973; Pyle 1989) rely on tephra fall layer features, such as dispersal, thinning rate, volume, etc. Pyroclastic fall (PFall) deposits are also used to investigate generation, transport and sedimentation of the particles to get a better insight into eruptive dynamics in the conduit and at the vent (Rose et al. 2008; Carey et al. 2009; Arana-Salinas et al. 2010; Carey and Houghton 2010). Compilations of many grain-size analyses of tephra have shown that most fall deposit layers are characterized by fairly unimodal, log-normal distributions, with good to very good sorting for a pyroclastic deposit, i.e. σ_{Φ} defined by $(Q_{84} - Q_{16})/2$ (Inman 1952) typically between 0.5 and 2.5 (Walker 1971). However, more recent studies have revealed discrepancies to this common feature. For example, near-to-vent coarse-grained fall deposits may show mixing of ballistic and plume-derived clasts, yielding polymodal grain-size distributions (Fierstein et al. 1997; Houghton et al. 2004). Similarly, Brazier et al. (1983) highlighted the influence of ash aggregation processes in volcanic plumes, notably on the decay rate of the Mt. St. Helens ash layer (secondary thickening) and its multimodal grain-size distributions. Walker (1981a, b) reported the enrichment of fine particles in an ash deposit from the Taupo volcano (New Zealand) by early sedimentation prompted by rain-flushing. Departures from simple, Gaussian-like distributions have thus been widely documented in fine-grained, ash-grade tephra fall deposits (Walker 1981b; Darteville et al. 2002; Evans et al. 2009; Rose and Durant 2009). Between these grain-size end-members, i.e. in the lapilli-dominated size range, deviation from a bell-shaped distribution has been rarely documented.

In this paper, we focus on the pyroclastic fall layer emplaced during the August 16–17, 2006 paroxysmal eruption of the Tungurahua volcano (Ecuador). This andesitic eruption lasted for approximately 9 h, with 6 h of paroxysmal activity, during which a column rose up to more than 15 km above the crater, drifted West and produced a dark-toned scoria and ashfall layer in the Inter-Andean highlands, while numerous pyroclastic flows (PF) descended the northern, western and southern flanks of the volcano. Thinning rates and tephra volumes are calculated to infer the size of the August 2006 eruption, notably the Volcanic Explosivity Index (VEI). In addition, we investigate grain-size distributions of the pyroclastic fall layer to obtain a fragmentation index and infer the eruption type and to decipher the origin of grain-size complexities in lapilli-sized tephra fall deposits, using improved deconvolution techniques. Overall, our work provides the first

ground-based analysis of this violent and destructive eruption, which claimed six lives in the southern area of the volcano.

Geological setting and recent volcanic activity

Tungurahua is a 5,023-m high andesitic stratovolcano located in the southern part of the Eastern Andean Cordillera of Ecuador, about 120 km south of Quito (Fig. 1a, b). It is a steep-sloped volcano surrounded by three main rivers named Puela, Chambo and Pastaza, which have excavated deep gorges on its south, west and north bases, respectively (Fig. 1c). It is one of the most active volcanoes in Ecuador, with an activity usually located at the summit crater (Barberi et al. 1988; Hall et al. 1999; Le Pennec et al. 2006). Geochronological studies show evidence of frequent pyroclastic density currents, lava flows, ash fall and lahars in the past millennium, mainly emplaced in the 3,000-year-old amphitheatre carved in the western flank of the edifice (Hall et al. 1999; Molina et al. 2005; Le Pennec et al. 2008). A recurrence rate of at least one pyroclastic flow-forming eruption per century has been estimated (Le Pennec et al. 2006, 2008). More than 25,000 inhabitants living near the volcano are threatened by pyroclastic flows and lahars, and most of the local rural population cultivates land in areas frequently affected by ash falls and acid rains (Le Pennec et al., personal communication).

Tungurahua began a new eruptive period in 1999, after 80 years of dormancy. Since then, the activity has fluctuated with phases of uneven intensity, size (VEI 1 to VEI 3) and style (strombolian, vulcanian, subplinian), while eruptive products have shown monotonous andesitic compositions (58–59 wt.% SiO₂; Samaniego et al. 2011). Intense eruptive phases have occurred, e.g. in November–December 1999, August 2001, July 2006, August 2006, February 2008, May and December 2010. The most powerful phase took place on August 16–17, 2006, claiming six lives and destroying houses, roads and crops. Apart from these paroxysmal events, the usual activity since 1999 has been characterized by low to moderate explosive phases of strombolian style, with short-lived explosions and ash plume below 3 km above the crater. These explosive phases were separated by periods of quiescence, notably from February to December 2005. From this time on, the activity progressively intensified and culminated with the July 14, 2006 eruption: for the first time since the 1999 reawakening, a highly explosive event took place, with pyroclastic flows reaching the base of the edifice. After this phase, the activity progressively decreased to a moderate level for about 1 month, with frequent ash and gas emissions.

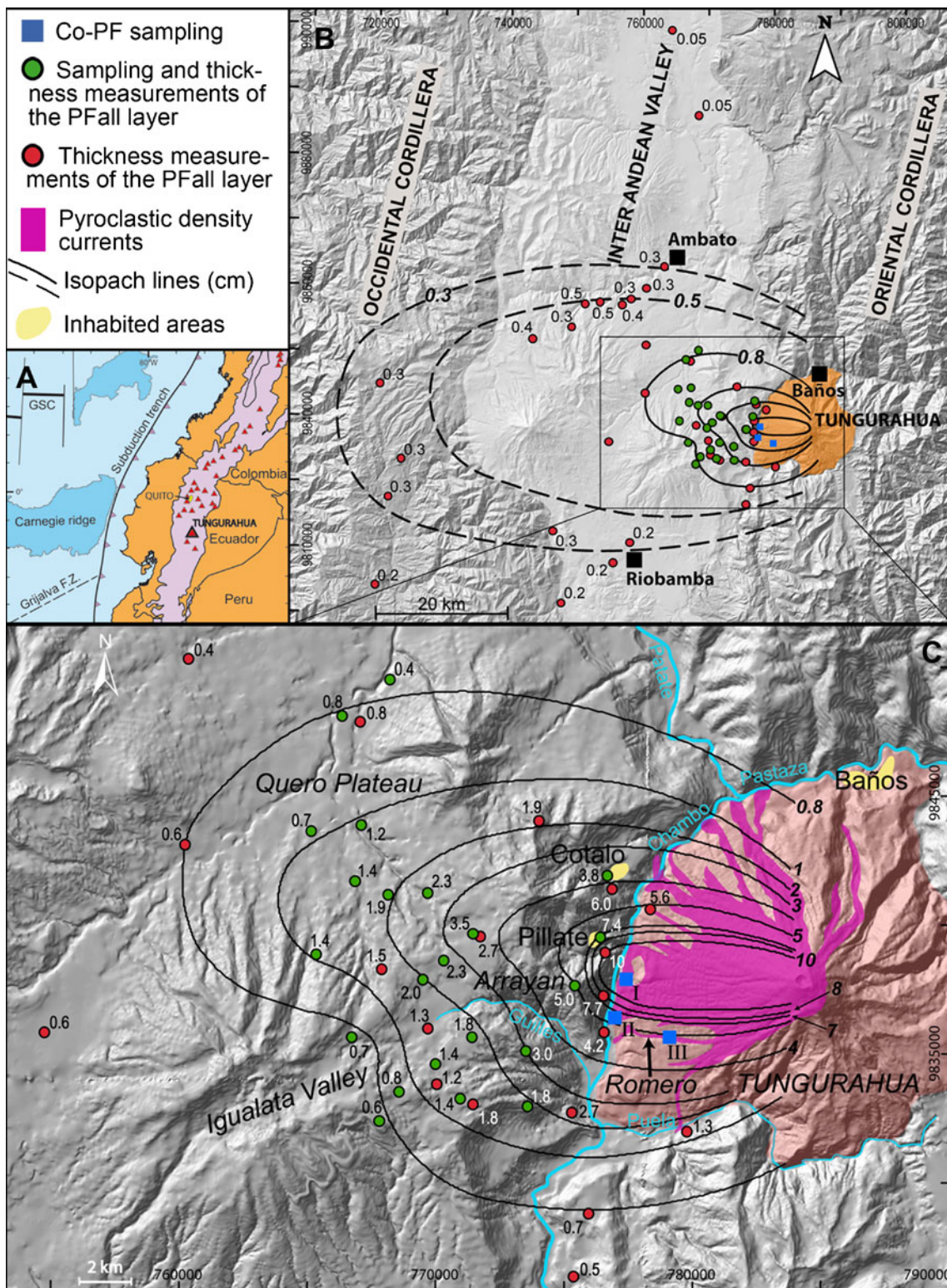


Fig. 1 **a** Location map of the Tungurahua volcano in Ecuador. **b** Area of sampling and thickness measurements of the Pfall layer from the August 2006 eruption. **c** Map of the proximal depositional area showing the distribution of pyroclastic density current deposits (after Kelfoun et al. 2009). The sampling locations of the Co-pyroclastic

flow deposits are labeled from I to III. **b, c** Numerical labels thickness values in centimetres. *Solid lines* isopach contours of the Pfall layer in centimetres (*dashed lines* for distal isopachs). *Red dots* sites of thickness measurements only. *Green dots* sites of thickness measurements and tephra sampling

On the morning of August 16, seismic activity increased. A persistent column reached 3 km above the crater, and the plume drifted West and North-West. The first small pyroclastic flows descended the north-west flank at 2200 hours UTC (UTC=local time+5). During the next hours, the activity continued to increase and reached its climax at about 0515 hours UTC on August 17 and lasted approximately 50–60 min: powerful and persistent incandescent jets rose up to 1 km above the crater, numerous pyroclastic flows rushed down to the rivers surrounding the volcano (Kelfoun et al. 2009) (Fig. 1c), a sustained SO₂-rich eruption column reached a height >15 km above the summit and the plume spread over the Inter-Andean Valley, west of the volcano, and the Pacific Ocean (Arellano et al. 2008; Kelfoun et al. 2009; Steffke et al. 2010; Samaniego et al. 2011) (Fig. 1a, b). From 0700 hours UTC on August 17, the seismic and eruptive activities decreased abruptly, and the emission of pyroclastic flows ended. On August 17, andesitic lava flowed down the western flank, and tephra fall was restricted to the proximal area west of the volcano. Petrological investigations (Samaniego et al. 2011) show that the August 2006 eruption was triggered by a massive injection of a gas-rich andesitic magma into the deep plumbing system, followed by a rapid ascent to the surface, thus enhancing explosivity. In this paper, we focus on the 2006 pyroclastic deposits of the August 16 event, with emphasis on the fall layers deposited on the Quero Plateau, an area located 7 to 20 km from the volcano (Fig. 1b, c).

Stratigraphy and sampling

The stratigraphy, lithological features and characteristics of the pyroclastic deposits are summarized in a synthetic log (Fig. 2), based on studies carried out at selected sites in the depositional area (Figs. 1c and 3).

Pyroclastic flow deposits

The PF deposits are concentrated in gullies on the lower western flank of the volcano and as large fans in the Chambo and Puela Rivers terraces (Fig. 1c). The deposits consist of juvenile blocks and moderately vesicular bombs scattered in a grey-toned matrix of lapilli and ash (Figs. 2 and 3). These PF breccias comprise multiple flow units locally showing an erosional basal surface. The total thickness varies from a few metres on the volcano's flanks to 20 m in the Chambo River terrace (Fig. 3). The composition (58–59 wt.% SiO₂; Samaniego et al. 2011) and the texture of the juvenile elements, along with geometric and facies characteristics, indicate that these

deposits are typical block-and-ash scoria flow deposits (Freundt et al. 2000).

Pyroclastic surge deposits

The pyroclastic surge (PS) deposits are commonly less than 50 cm thick and are fine-grained (median grain size ~63 μm), well-sorted ash beds showing dune bedding and/or planar stratifications (Fig. 2). They cover the PF deposits in most places and locally occur as discontinuous and truncated beds between the PF sub-units (e.g. section III_a in Fig. 3). The PS deposits also occur upon interfluvial areas where they display overbank facies that extend several tens to hundreds of metres away from the gullies where coarse-grained PF were emplaced. The vertical and lateral transitions from PF to PS deposits are gradational, with a decrease in grain-size and an improvement of the sorting at the layer scale (Figs. 2 and 3).

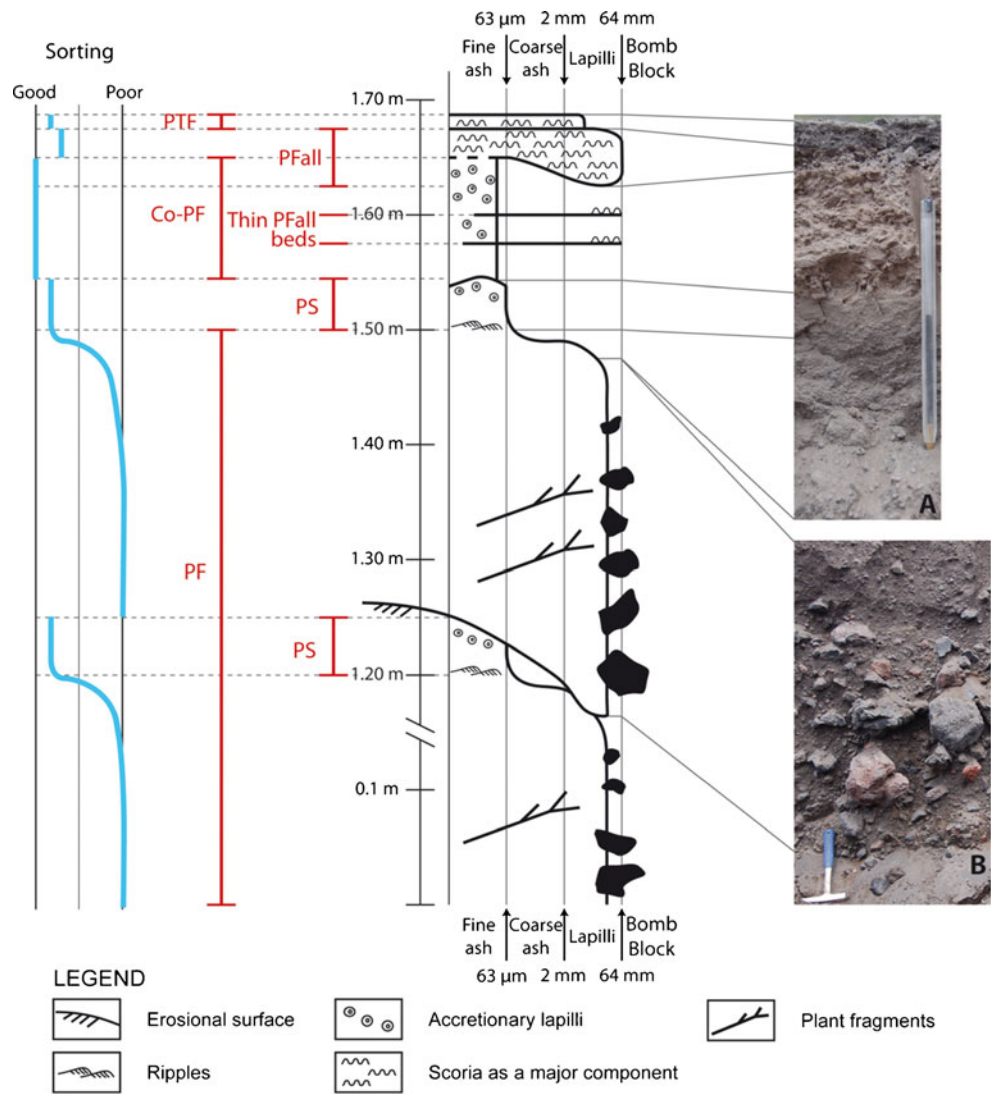
Co-pyroclastic flow deposits

At many localities (Fig. 3), the PF and PS deposits are covered by massive, well sorted and very fine-grained (median grain size ~40 μm) ash beds, from a few millimetres to 20 cm in thickness, containing numerous accretionary lapilli (Fig. 2a). These stratigraphic and lithological features suggest that these massive ash beds are Co-pyroclastic flow (Co-PF) deposits (Fig. 2). Co-PF, as defined by Sparks et al. (1973), Bonadonna et al. (2002) and Evans et al. (2009), are turbulent ash clouds that develop during the elutriation of fine-grained particles produced by comminution in moving pyroclastic density currents.

The pyroclastic fall layer

The PFall layer is a non- to lightly stratified, brown andesitic scoria bed containing a small proportion (1–2%) of white silicic pumice clasts (60–66 wt.% SiO₂ according to Samaniego et al. (2011)) and scattered lithic fragments, deposited as a large sheet over more than 3,000 km² across the Inter-Andean Valley. In the depositional area of the pyroclastic density currents (i.e. on the flanks of the volcano and in Chambo and Puela gorges, Fig. 1c), the PFall layer is a lapilli-grade and well-sorted deposit consisting of: (1) <0.5–4-cm thick bed occurring at the top of the eruptive sequence and (2) 1–2-mm thick beds intercalated within the Co-PF and locally PF and PS deposits (Figs. 2 and 3). On the Quero Plateau, i.e. outside of the PF depositional area (Fig. 1c), the PFall layer is a single sub-massive, poorly to moderately sorted deposit of brown scoria lapilli containing a significant proportion of fine-grained ash (<63 μm).

Fig. 2 Synthetic log of the pyroclastic deposits of the August 2006 eruption of Tungurahua. The *horizontal scale* is based on the grain size of the deposits. *PF* pyroclastic flow deposits, *PS* pyroclastic surge deposit, *Co-PF* Co-Pyroclastic flow deposit, *Pfall* pyroclastic fall deposit, *Thin Pfall beds* series of intercalated 1–2-mm thick Pfall beds, *PTF* tephra fall deposit post-August 2006. **a** Photograph of the pyroclastic sequence at location I. **b** Photograph of coarse PF deposits in the Romero gully (location III)



Sampling and thickness measurements

The Co-PF deposits were sampled at three sites on the western flank of the volcano (locations I, II and III in Figs. 1c and 3). At site III, we studied and sampled three sections (III_a, III_b and III_c on Fig. 3) located upon a terrace at 15, 31 and 121 m from the Romero ravine, which hosts the PF deposits. At locations III_b and III_c, the Co-PF layers are intercalated with numerous 1–2-mm thick tephra fall beds, thus making the sampling difficult.

Because of the intercalation of the Pfall layer with PF, PS and Co-PF deposits, reliable Pfall thickness was difficult to measure in the PF depositional area (0–7 km from the crater east of the Chambo river; Fig. 1c). We obtained 59 thickness measurements outside of the PF depositional area, from 7 to 60 km from the vent, mainly on the Quero Plateau (Fig. 1b, Table 1S in Electronic Supplementary Material (ESM)). We also collected 22 samples in

the area located between 7 and 20 km from the vent (sites displayed as green dots in Fig. 1c, Table 1S in ESM) in order to perform the analyses presented below.

Estimation of the eruption parameters

Tephra dispersal and volume estimate of the Pfall layer

The thickness data were plotted on a map (Figs. 1a and b) where nine isopachs in the range 0.8–10 cm were contoured with satisfactory precision, while two additional lines for 0.3 and 0.5 cm were drawn in distal areas despite fewer thickness constraints. The map shows a dispersal axis towards the West defining a main lobe on the Quero Plateau, and a local irregularity of the shape of isopachs' contours isolating a secondary lobe south-west of the volcano between Guilles and Igualata valleys (Fig. 1c). A

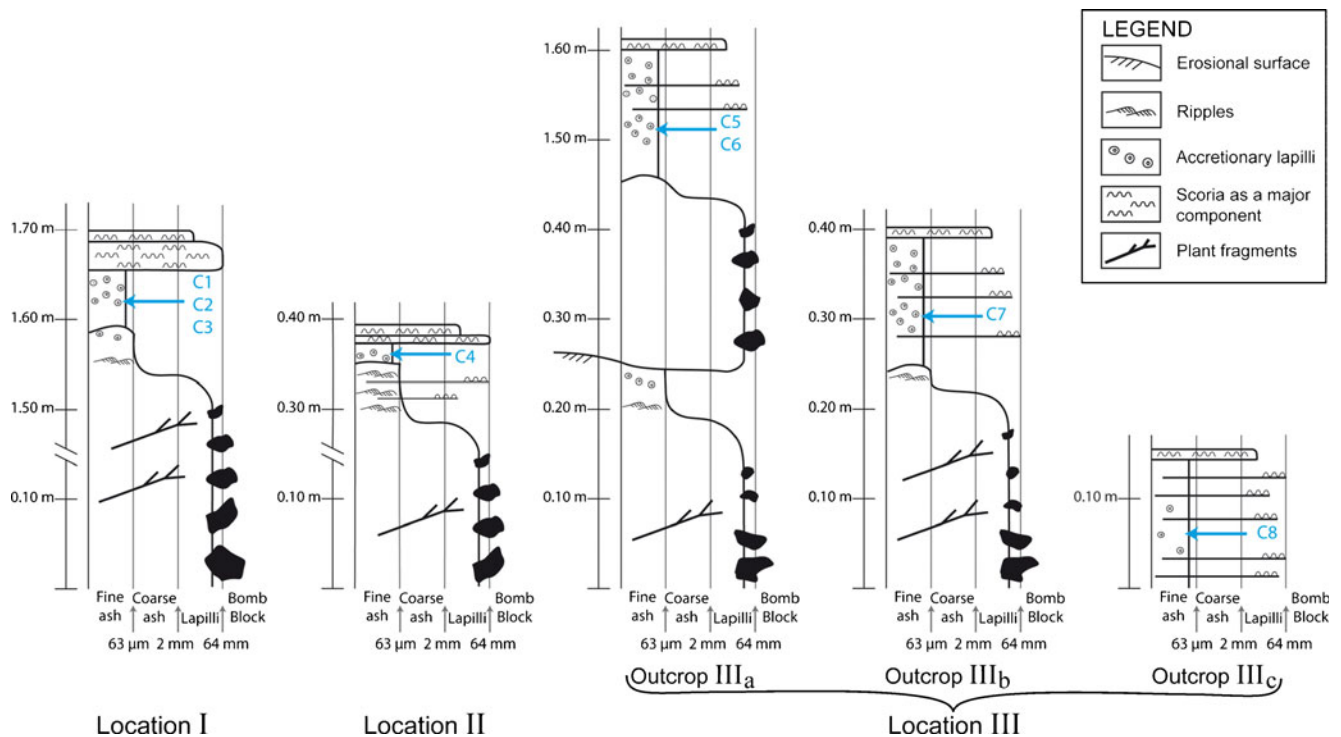


Fig. 3 Stratigraphic logs of pyroclastic sequences at locations of Co-PF sampling. Location of sections *I*, *II* and *III* is shown in Fig. 1c. The locations *III_a*, *III_b* and *III_c* are situated at 15, 31 and 121 m,

respectively, away from the Romero gully where dense PF were deposited (Fig. 1c). The stratigraphic position of the eight samples of Co-PF is reported in each log (C1–C8)

plot of the logarithm of the tephra thickness (*T*) versus the square root of isopach area (\sqrt{A}) (Pyle 1989; Fierstein and Nathenson 1992; Bonadonna et al. 1998) documents the thinning rate of the deposit and shows that our data are well fitted by an exponential law with two breaks-in-slope and also by a power law (Fig. 4). Such mathematical expressions, as given below in Eqs. 1 and 2 for exponential and

power laws, respectively, describe reasonably the decay rate of many other well-documented fallout deposits (Bonadonna and Houghton 2005; Rose et al 2008; Carey et al. 2009; Costantini et al. 2009; Watt et al. 2009) .

$$T = T_0 \exp(-k\sqrt{A}) \tag{1}$$

$$T = T_{pl}A^{-m/2} \tag{2}$$

where *T* is the thickness of the deposit, *T*₀ is the extrapolated thickness at the vent, *A* is the isopach area, *k* is the slope of the exponential law, *T*_{pl} is the power-law parameter and *m* is the power-law exponent. The parameters and the coefficients of determination (*R*²) obtained for our data collection are reported on Fig. 4.

We calculated the bulk volume of the Pfall layer by integrating the laws over given intervals (Fierstein and Nathenson 1992; Bonadonna et al. 1998; Bonadonna and Houghton 2005), and the results are given in Table 1. For the exponential thinning rate, we integrated the three segments and obtained a volume of 42 × 10⁶ m³. Because the power law converges neither to zero nor to infinity, we integrated from 1 m to 100 km and from 1 m to 200 km, to obtain volumes of 37 and 57 × 10⁶ m³, respectively. The distance of 100 km to the West coincides with the western border of the Occidental Cordillera, while 200 km to the

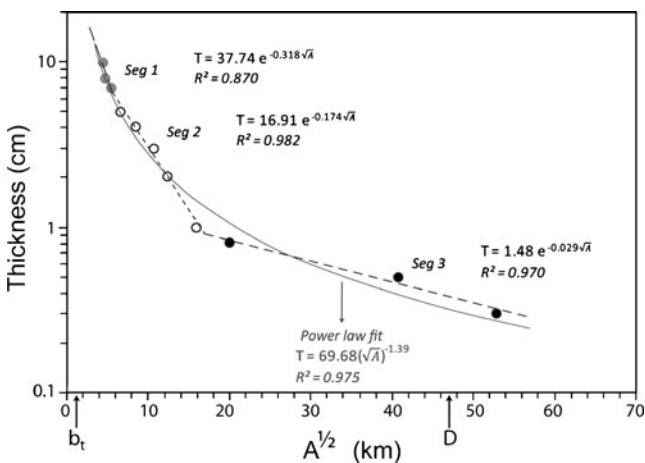


Fig. 4 Semi-log plot of thickness vs. (isopach area)^{1/2} for the Pfall layer of the August 2006 eruption of Tungurahua. *Solid curve* power law fit, *dashed lines* the three segments of the exponential fit with two breaks in slope, *D* dispersion index after Walker (1973), *b_t* the thickness half distance after Pyle (1989)

Table 1 PFall deposit volumes calculated from the two mathematical laws fitting the thinning rate of the PFall layer

Mathematical fit	Integration interval (m)	Volume (10^6 m^3)
Exponential Law (3 breaks-in-slope)	[0.38; $+\infty$]	42.0
Power Law	[1; 100,000]	37.2
Power Law	[1; 120,000]	41.6
Power Law	[1; 150,000]	47.6
Power Law	[1; 200,000]	56.6

West matches the Ecuadorian coast. These results indicate that the volume estimated with the power law fit is close to that obtained with the three-segmented exponential decay rate, when the integration is bounded to 120 km ($42 \times 10^6 \text{ m}^3$), which means that both models yield a similar result when the volume beyond the ~ 0.9 mm isopach is neglected in the power law integration. Both volume estimates are to be considered as minimum volumes as they do not include the distal ash volume (Sulpizio 2005; Rose and Durant 2009). The maximum volume of the PFall deposit is considered as a continuous layer as far as the Pacific Ocean, where the thickness calculated using the power law decay rate would be more than 0.04 cm, which yields a volume of $57 \times 10^6 \text{ m}^3$ (Table 1).

These results also show that when thickness data are available to draw a third exponential segment in the graph T vs. \sqrt{A} , as is usually the case for recent well-documented eruptions, the exponential law with two breaks-in-slope is close to the power law as it represents fairly well the distal thinning rate (Fig. 4).

Eruptive column height

The maximum column height is estimated from an isopleth map (Fig. 5a) of scoria clasts by applying the methods of Carey and Sparks (1986) and Pyle (1989). The maximum size of the scoria clasts (MSS) is calculated from the average of the three principal diameters of the five largest fragments, which yields the volume of the clasts by approximation as an equivalent ellipsoid. After dry weighing, a mean scoria density of $\sim 600 \text{ kg/m}^3$ is found. Carey and Sparks' method is based on the extent of downwind and crosswind axes of the isopleths and our data point to a maximum column height of ~ 16 km above the vent. Using an empirical expression, Pyle's method determines a value for the neutral buoyancy height (H_B) from the slope of the fit in the plot MSS vs. $\sqrt{\text{Isopleth Area}}$ (Fig. 5b). This yields a column height of ~ 18 km above the vent (Fig. 1c). Steffke et al. (2010) infer a plume height of 24 km a.s.l. from satellite remote sensing data using plume top temperature and velocity determination methods.

Grain-size analyses and deconvolution

Techniques for grain-size analyses

Grain-size analyses of the 22 PFall samples were carried out from -5 to 10Φ (i.e. from 31.5 mm to $1 \mu\text{m}$, with $\Phi = -\log_2 d$, d being the particle diameter in millimetres). We combined the mechanical sieving method at a $0.5\text{-}\Phi$ interval from -5 to 4Φ (31.5 mm– $63 \mu\text{m}$) and the laser diffraction method beyond 4Φ , with an overlap of both analytical techniques between 3.5 and 4Φ (90 and $63 \mu\text{m}$, respectively) for 19 samples, and between 3 and 4Φ (125 and $63 \mu\text{m}$) for 3 samples. Each granulometric fraction of tephra was weighed at 10^{-2} g. Laser diffraction measurements were performed with a Malvern Mastersizer S instrument at the CEREGE Research Center (Aix-en-Provence, France). About 0.2 g of the selected cumulative fraction (for example, the fraction finer than 3.5Φ) was dispersed in 400 mL of water, and three to five measurements were obtained for each sample.

All Co-PF samples were analyzed using the laser diffraction method with a dry dispersion system on a Malvern Mastersizer S at the ENSCCF Upper Chemical School (Blaise Pascal University, Clermont-Ferrand, France). For each sample, grain-size analyses were carried out from 0 to 10Φ (1 mm to $1 \mu\text{m}$) and duplicated.

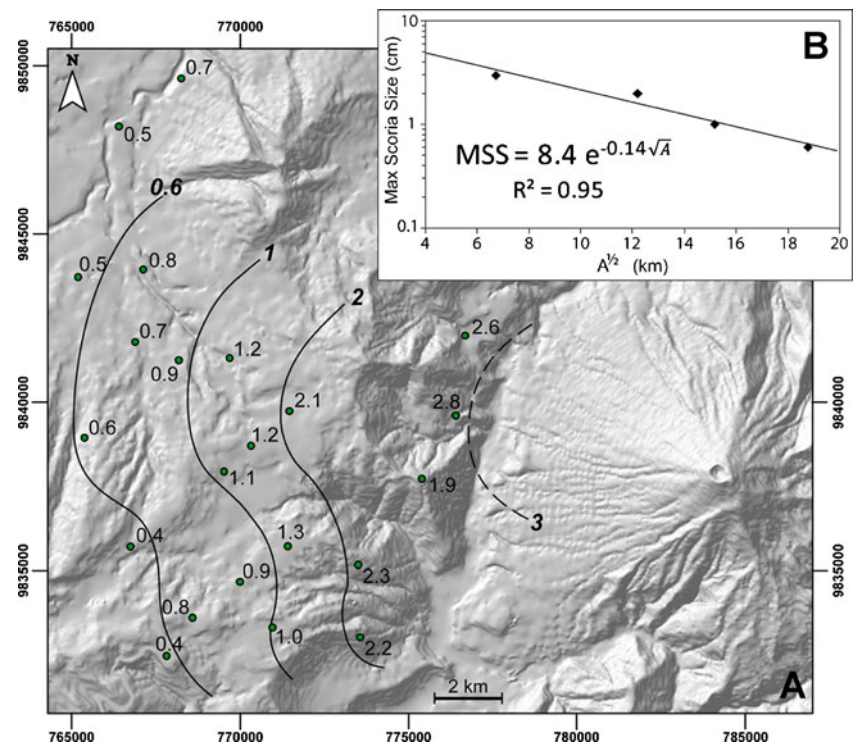
Reconstructing grain-size distributions of PFall and Co-PF samples

Grain-size distributions obtained from sieving are in weight percentage on a $0.5\text{-}\Phi$ interval scale. Laser diffraction results are in volume percentage on a discrete scale with bins of approximately 0.2Φ . We merged several fractions to obtain a consistent 0.5Φ scale from -5 to 10Φ , assuming that the volume percentage varies linearly in a $0.2\text{-}\Phi$ interval in the laser diffraction size range. Because of particle shape irregularities, distributions from laser diffraction do not match exactly at the sieve size limit (90 or $125 \mu\text{m}$). Thus, after several iterations, we set an empirical threshold in laser diffraction data to match laser with sieving data in the overlapping size range.

For the 22 ash samples, grain-size distributions obtained by mechanical sieving and laser diffraction were merged together using a volume-to-mass conversion based on two assumptions: (1) for the laser diffraction analysis, a representative volume of grains is selected in the grain-size fraction of the sample, (2) grain density inhomogeneity in each grain-size fractions from 3.5 to 10Φ is assumed to be negligible. With these assumptions in mind, the weight percentage of a grain-size fraction of a given size (X_f) is:

$$X_f = (x_f \times X_{<t}) / 100 \quad (3)$$

Fig. 5 **a** Isoleth map of the PFall layer, with contour lines labelled in centimetres. The mean value of the maximum size of the scoria clasts is given in centimetres. **b** Semi-log plot of the maximum size of the scoria clasts vs. (isopleths area)^{1/2} for the PFall layer



where x_f is the volume % of a granulometric fraction of a given size and $X_{<t}$ is the weight % (wt.%) of the cumulative grain-size fraction selected for the analysis (>3 or $>3.5 \Phi$). Thus, laser and sieving data were combined using the threshold value deduced from the laser diffraction data, and the whole grain-size distributions in weight % were reconstructed from -5 to 10Φ with steps of 0.5Φ .

All samples from the Co-PF deposits were analyzed using the laser diffraction method, in the size range 0 – 10Φ (1 mm to $1 \mu\text{m}$) and converted on a 0.5Φ scale by gathering fractions with $\sim 0.2 \Phi$ bins. We simply converted the volume % to weight % assuming similar grain density in all fractions from 1 to 10Φ .

Deconvolution of polymodal distributions

A few reconstructed distributions are unimodal while most are polymodal (see “Results”), with typically two or three modes and skewed tails. Because the interpretation of such complex distributions is not straightforward, we developed a deconvolution procedure which converts polymodal populations to unimodal subpopulations, using the LOGN_2D algorithm (Appendix). The algorithm is based on the discretized Weibull-type distribution (Gouhier and Donnadiou 2008), and it minimizes the number of subpopulations to the number of modes identified in the distribution in the case of non-log-normal distributions. The flexibility of the Weibull distribution enables easy interpolation within a wide range of probability density functions (e.g. exponential,

Gaussian, log-normal) and allows the fit of positively skewed distributions, a situation that is not achievable with SFT software of Wohletz et al. (1989). Such processing yields improved fits to our data compared to SFT software results and thus offers a better insight into dispersal and transport mechanisms. The deconvolution principle is exemplified in Fig. 6 for three selected samples, and the relevance of the protocol is detailed in Appendix.

Results

Grain-size distributions of the PFall layer

The grain-size distributions of the 22 samples from the PFall layer are bimodal (Figs. 7 and 8), with one mode coarser than 2Φ and another finer than 4Φ . One peak is mainly apparent in the laser sieving range but extends into the mechanical sieving range, thus indicating that the fine mode is not an artefact resulting from combination of mechanical and laser diffraction techniques. Grain-size distribution patterns displayed in Fig. 7 allow us to qualitatively distinguish four groups: (1) group A (as indexed in Fig. 7) comprises poorly sorted multimodal distributions, (2) group B includes sub-symmetrical distributions with two modes peaking at similar weight %, (3) group C consists of distributions with a coarse poorly sorted subpopulation and a smaller fine-grained subpopulation, (4) group D encompasses well-sorted distributions with a prominent coarse mode and a modest fine

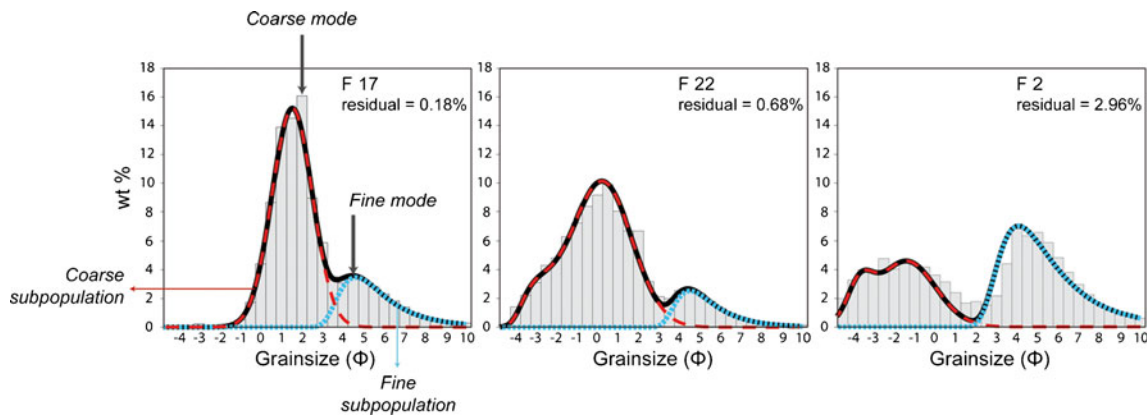


Fig. 6 Example of the deconvolution of three representative Pfall grain-size distributions. The subpopulations are calculated from the two main modes of the original distributions. *Dashed and dotted*

curves are coarse and fine subpopulations, respectively. *Thick solid curves* synthetic bimodal distributions resulting from the deconvolution procedure

subpopulation. Figure 8 shows that the samples from group A are located in the proximal zones; the samples from groups B and D occur close to the main dispersal axis and on the “wings” of the deposit, respectively; the samples from group C occur in the secondary lobe of the isopachs, south-west of the volcano.

The grain-size distributions are described here using parameters defined by Inman (1952): the median grain-size (Md_{Φ}), the sorting (σ_{Φ}) and the skewness (Sk) (Table 2). A graph of Md_{Φ} vs. σ_{Φ} (Fig. 9a) reveals that our data for bulk grain-size distributions plot dominantly into the field of pyroclastic flow deposits, with some data inside the tephra fall field, as delineated by Walker (1971).

To account for the bimodal grain-size pattern evidenced in Fig. 7, we deconvoluted all distributions to isolate two grain-size subpopulations using the procedure described above (Fig. 6, Appendix). Then, the distribution of each subpopulation was characterized separately using Inman’s parameters (Fig. 9 and Table 2). For the coarse subpopulation, Md_{Φ} ranges between -2.0 and 1.5Φ , σ_{Φ} between 0.7 and 1.9 and Sk between 0.02 and -0.15 . For the fine subpopulation, Md_{Φ} ranges between 1.7 and 1.2Φ , σ_{Φ} between 5.1 and 4.0 and Sk between 0.24 and 0.17 . σ_{Φ} of the coarse subpopulation tends to improve with decreasing Md_{Φ} , while σ_{Φ} of the fine subpopulation shows no clear correlation with Md_{Φ} (Fig. 9a). Md_{Φ} of the coarse subpopulation strongly correlates with the thickness, whereas Md_{Φ} of the fine subpopulation remains sub-constant over the whole Quero Plateau area (Fig. 9b). σ_{Φ} of the coarse subpopulation improves with the thinning of the deposit, while σ_{Φ} of the fine subpopulation remains similar regardless of thickness variations (Fig. 9c). According to the values of Sk, most coarse subpopulations are symmetrical (log-normal) and others are coarse-skewed (e.g. F 20, F 22), while all the fine subpopulations are fine-skewed (Table 2).

Grain-size distributions of the Co-PF deposit

The grain-size distributions of most samples from Co-PF deposits have a single mode between 4.5 and 5.0Φ (Fig. 10), and only two distributions needed to be deconvoluted. Indeed, as described in “Stratigraphy and sampling”, Co-PF deposits observed in sections III_b and III_c (31 and 121 m away from the Romero gully, Figs. 1c and 3) appeared intercalated with numerous Pfall beds. As a result, the samples collected (C7 and C8, Fig. 3) were slightly mixed with Pfall material, with implications for their grain-size distributions (Fig. 10): the distribution of the sample C8 reveals a minor and coarser mode at 1.5Φ , and the distribution of the sample C7 shows a “bulge” in the coarse fraction and a mode around 4.0Φ . These distributions were thus deconvoluted to isolate the finest subpopulation in the deposit.

Table 2 summarizes the grain-size results obtained for the Co-PF distributions. Md_{Φ} calculated from the unimodal distributions varies between 5.0 and 4.4Φ , σ_{Φ} between 1.6 and 1.8 and Sk between 0.15 and -0.08 . Md_{Φ} calculated for the fine subpopulations obtained by deconvolution of the distributions of samples C7 and C8 is 4.2Φ and 5.0Φ , σ_{Φ} is 1.7 and 1.8 and Sk is 0.23 and 0.08 , respectively. These values are similar to those obtained for the fine grain-size subpopulation identified in the Pfall samples, and the data plot in the same field in the graph Md_{Φ} vs. σ_{Φ} (Fig. 9a).

Discussion

Size of the August 16, 2006 eruption

Our volume estimates yield a rain-compacted tephra fall volume of about $42 \times 10^6 \text{ m}^3$ and previous studies have estimated the volume of bulk PF deposits at $5\text{--}10 \times 10^6 \text{ m}^3$ (Hall et al. 2007; Kelfoun et al. 2009). Therefore, the

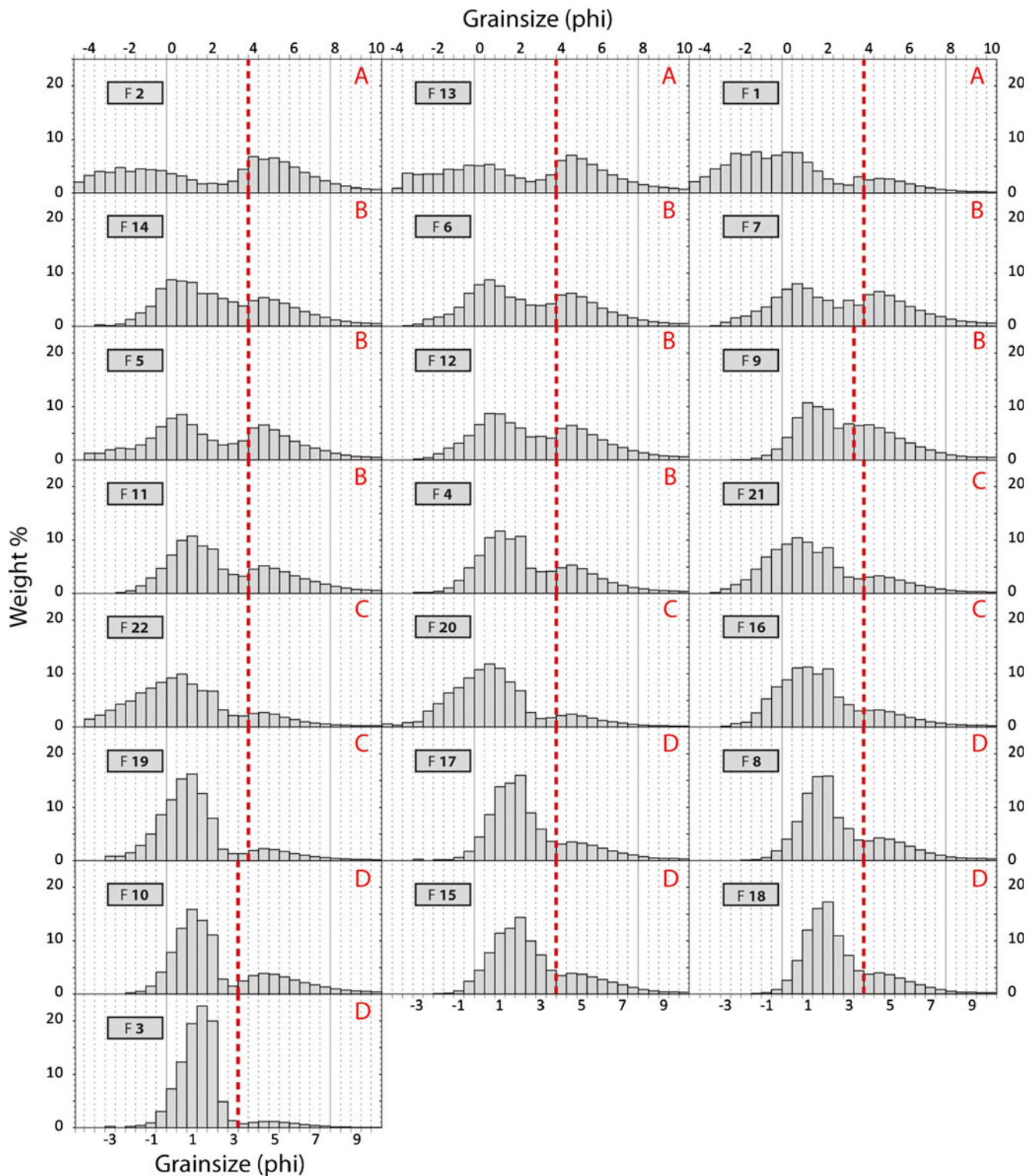
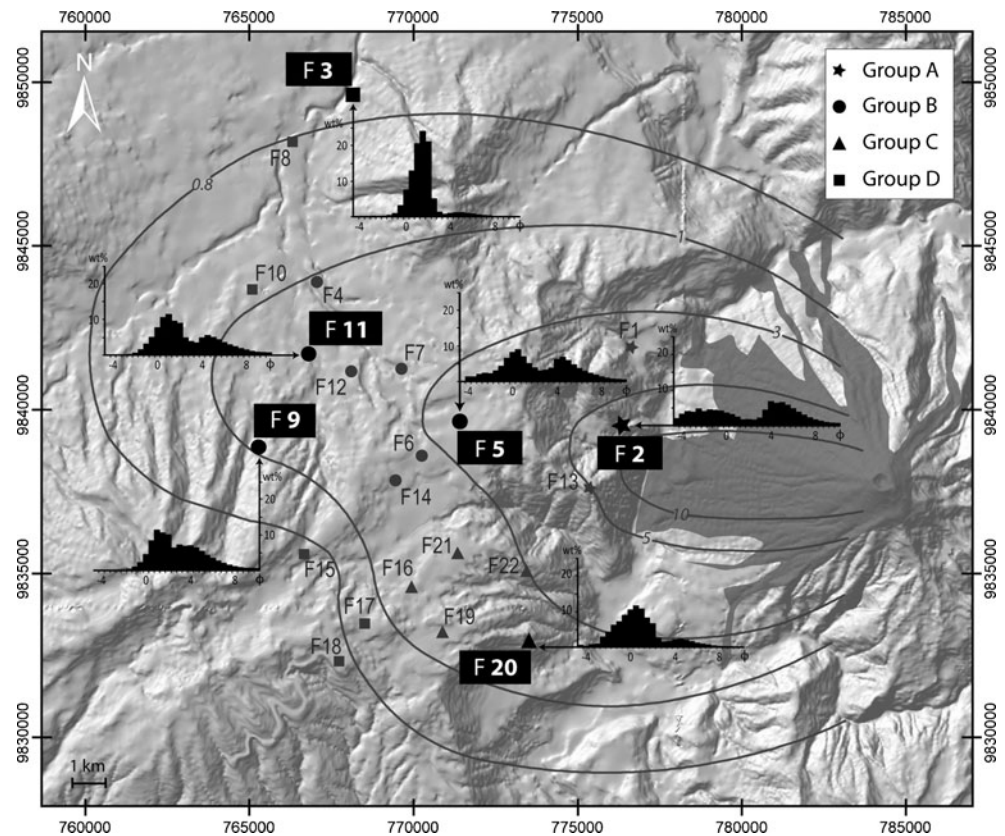


Fig. 7 Grain-size distributions of the 22 samples of the PFall layer in weight %. The *thick dashed line* is the limit between sieving and laser diffraction data. The distributions are classified in four groups (*A*, *B*, *C* and *D*) based on broad distribution features (see “Results”)

minimum tephra volume is $47 \times 10^6 \text{ m}^3$, and the maximum does not exceed $67 \times 10^6 \text{ m}^3$ (Table 1). In the VEI classification scheme of Newhall and Self (1982), these values rank the August 2006 phase at VEI 3, which differs

from the VEI 4 obtained by Fee et al. (2010), based on eruption duration and column height estimated from satellite-based data (Steffke et al. 2010). However, estimation of VEI solely from plume height may be insufficiently

Fig. 8 Representative grain-size distributions of PFall samples in selected places of the deposit. The *solid curves* are the isopach contours in cm. *Solid stars* locations of group A samples. *Solid dots* locations of group B samples. *Solid triangles* locations of group C samples. *Solid squares* locations of group D samples. The name of each sample is given on the map



precise for assessment of the size of a volcanic eruption. Indeed, local atmospheric conditions may have a strong influence on the plume height (rain scavenging, complex wind pattern, etc.). Moreover, assessment of plume height using either satellite or ground-based data remains a difficult task. In a satellite-based approach, plume height estimates using plume top temperature and wind velocity methods may be inaccurate because they require input parameters derived from atmospheric models. In deposit-based studies, the plume height determinations strongly depend on the amount of maximum size data and the resolution of the isopleth map (Biass and Bonadonna 2010). An estimate of the VEI based on the volume of the tephra deposit is much more reliable, and we rank the August 2006 phase as a VEI 3.

Origin of the grain-size subpopulations in the PFall layer

Our grain-size results reveal a bimodal distribution of all the samples collected in the Quero Plateau. The coarse-grained subpopulation is characterized by a decrease of Md_{ϕ} and an improvement of σ_{ϕ} radially away from source (Figs. 8, 9b, c). This pattern reflects the weight-driven fractionation of the particles in the plume, for which high to moderate Reynold numbers imply a dominantly exponential thinning rate: the coarsest particles settled early during plume dispersion, while fine ash particles had a longer

atmospheric residence time and settled beyond the sampling area. The coarse subpopulation of the PFall layer's grain-size distributions is therefore characteristic of a tephra fall deposit from a spreading volcanic plume fed by a sustained column (Fisher 1964).

The grain-size characteristics of the fine subpopulation in our samples from the PFall layer suggest different transportation and sedimentation processes as compared to the coarse subpopulation: (1) Md_{ϕ} and σ_{ϕ} show no correlation with the thinning of the deposit (Figs. 9b, c), (2) all distributions display a positive skewness (Fig. 7 and Table 2), (3) in Walker's plot of σ_{ϕ} vs. Md_{ϕ} (Fig. 9a), the grain-size distributions of the fine subpopulation have a fallout signature, (4) in the same plot, σ_{ϕ} and Md_{ϕ} for the fine subpopulation of the PFall layer show values that are similar to those of the Co-PF deposit (Fig. 9a).

These grain-size characteristics of the fine subpopulation and particularly the constancy of Md_{ϕ} and σ_{ϕ} in the whole deposit cannot be explained by a rain-flushing process, i.e. the early fall of fine ash particles, precipitated by rain droplets from the plume, to the ground (Walker 1981b), because this process is plausible only locally as "muddy" ash fall was reported during the eruption only in the Pillate area (Fig. 1c). However, most witnesses west of the volcano indicated that the eruption took place in cloudy weather conditions but without rain at ground level. In addition, we found no evidence of ash aggregation in the tephra fall

Table 2 Calculated Inman's parameters of the grain-size distributions for samples from the Pfall layer and the Co-PF deposits. The two subpopulations were isolated using the deconvolution of the bulk bimodal distribution

Sample	Bulk distributions			Coarse subpopulation				Fine subpopulation			
	Md _Φ	σ _Φ	Sk	Mode	Md _Φ	σ _Φ	Sk	Mode	Md _Φ	σ _Φ	Sk
F 1	-0.5	3.2	0.26	-1.0	-1.2	1.8	0.02	4.0	4.4	1.6	0.24
F 2	2.7	4.3	-0.28	-1.4	-2.0	1.7	-0.03	4.1	4.6	1.7	0.20
F 3	1.1	0.9	-0.10	1.4	1.1	0.7	0.00	4.4	4.6	1.3	0.20
F 4	1.6	2.4	0.33	1.0	0.8	1.0	0.00	4.3	4.6	1.4	0.22
F 5	1.5	3.1	0.20	0.4	-0.1	1.5	-0.15	4.5	4.8	1.5	0.23
F 6	1.9	2.9	0.17	0.6	0.3	1.3	0.01	4.5	4.9	1.6	0.22
F 7	1.5	3.1	0.20	0.5	0.0	1.6	-0.14	4.4	4.8	1.5	0.19
F 8	1.8	2.0	0.41	1.6	1.4	0.9	0.02	4.8	5.1	1.4	0.19
F 9	2.3	2.3	0.21	1.2	1.0	0.8	0.01	3.6	4.0	1.5	0.22
F 10	1.3	2.3	0.49	1.0	0.7	0.8	-0.01	4.6	5.0	1.5	0.17
F 11	1.7	2.7	0.35	1.0	0.8	1.2	0.00	4.6	5.1	1.6	0.20
F 12	2.1	2.8	0.17	1.0	0.7	1.3	0.00	4.6	5.1	1.7	0.21
F 13	2.1	3.8	-0.04	-0.1	-0.7	1.9	-0.08	4.5	4.9	1.5	0.20
F 14	1.8	2.8	0.22	0.5	0.2	1.4	0.00	4.6	5.0	1.5	0.20
F 15	1.9	2.1	0.35	1.7	1.5	1.0	0.00	4.7	5.1	1.6	0.20
F 16	1.1	2.2	0.24	0.9	0.7	1.3	-0.01	4.5	4.8	1.3	0.19
F 17	1.7	1.9	0.38	1.5	1.3	1.0	0.00	4.6	5.0	1.4	0.19
F 18	1.8	1.8	0.38	1.8	1.5	0.8	-0.01	4.4	4.8	1.5	0.21
F 19	0.6	1.5	0.11	0.7	0.4	1.0	0.00	4.6	4.9	1.4	0.20
F 20	0.3	2.0	0.10	0.3	0.1	1.4	-0.01	4.5	4.8	1.2	0.20
F 21	0.8	2.5	0.28	0.5	0.2	1.4	0.00	4.6	4.8	1.4	0.23
F 22	0.2	2.5	0.15	0.2	-0.3	1.7	-0.09	4.5	4.8	1.3	0.20
C1	5.0	1.7	0.09								
C2	5.0	1.6	0.12								
C3	4.8	1.6	0.11								
C4	4.4	1.6	0.15								
C5	4.7	1.7	0.07								
C6	4.8	1.8	0.01								
C7	3.8	1.9	0.12	2.0	1.8	0.6	0.01	3.8	4.2	1.7	0.23
C8	4.6	2.3	-0.08	1.6	1.4	0.6	0.04	5.0	5.0	1.8	0.08

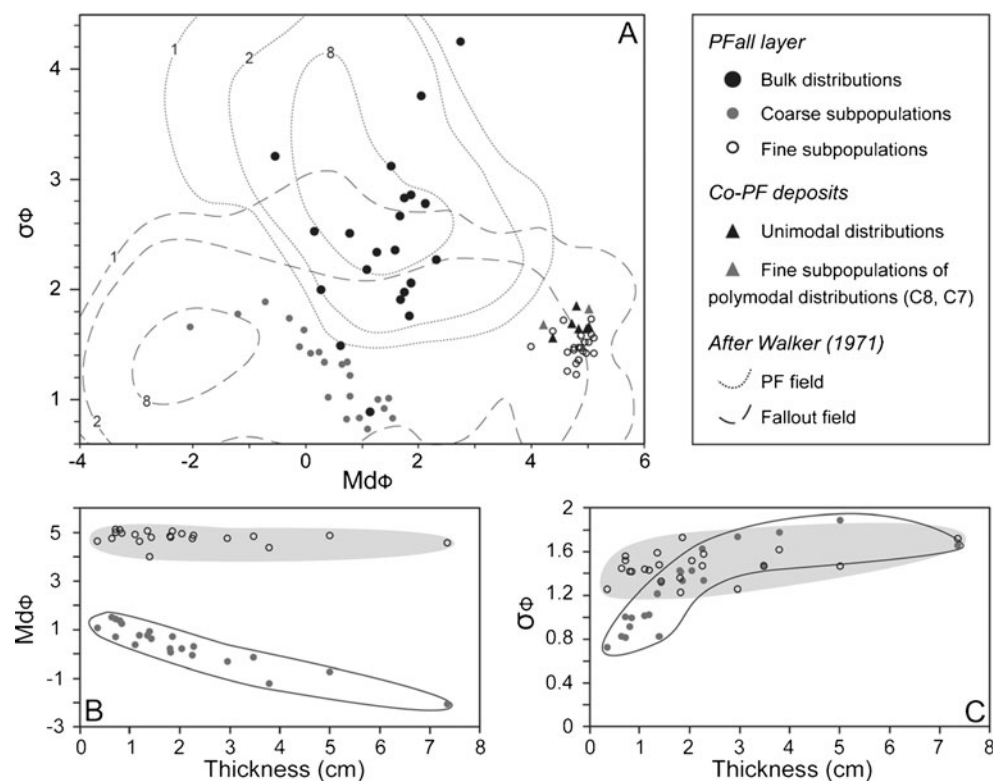
layer during field work and sampling. On the other hand, the grain-size distributions (Md_Φ, σ_Φ and Sk) of the Co-PF samples show close similarities with the fine subpopulation of the Pfall, which argues for comparable transport and sedimentation mechanisms. The positive skewness of the fine subpopulation supports a comminution process (Freundt and Schmincke 1992; Wohletz et al. 1989) during the PF emplacement: we interpret that the very fine particles (>7 Φ) constituting the tail of the distributions result from the milling of grains in coarser grain-size ranges. We infer that this grain-size subpopulation results dominantly from the settling of fine ash elutriated from moving scoria flows and transported over the Quero Plateau, largely beyond the PF depositional area. The process of elutriation above dense PF promotes the segregation of well sorted fine-grained fractions in Co-PF ash clouds (Evans et al. 2009; Rose and Durant 2009), and

due to their similar floatability, transport has little influence on grain-size distribution in the Co-PF cloud. Therefore, the resulting Co-PF ash deposit is expected to show similar median grain size and sorting regardless of the distance from the source.

Co-PF transport and deposition

In this section, we address the processes which caused synchronous deposition in the Pfall layer of: (1) coarse tephra fall particles from the plume and (2) the fine ash settled from the Co-PF clouds. The map in Fig. 11 shows the weight fraction of the fine subpopulation (x_{FS}) in the bulk grain-size distributions of the Pfall samples, according to the deconvolution procedure described in “Grain-size analyses and deconvolution” and Appendix. Noticeably, the region with x_{FS} values above 40% coincides with the

Fig. 9 Plots of the two subpopulations of the grain-size distributions of the 22 PFall layer samples. *Grey dots* coarse subpopulation, *open dots* fine subpopulation. **a** Plot of σ_Φ vs. Md_Φ for PFall and Co-PF data. *Solid dots* bulk distributions of PFall samples. *Solid triangles* unimodal grain-size distributions of the Co-PF deposit samples. *Open triangles* fine subpopulation of the distributions C8 and C7. Fallout field (*dashed line*) and pyroclastic flow field (*dotted line*) of Walker (1971) are shown for 1%, 2% and 8% contours. **b** Plot of Md_Φ vs. thickness of the deposit. **c** Plot of σ_Φ vs. thickness of the deposit. **a**, **b** Greyed and contoured fields display variation trends of the fine and coarse subpopulations, respectively

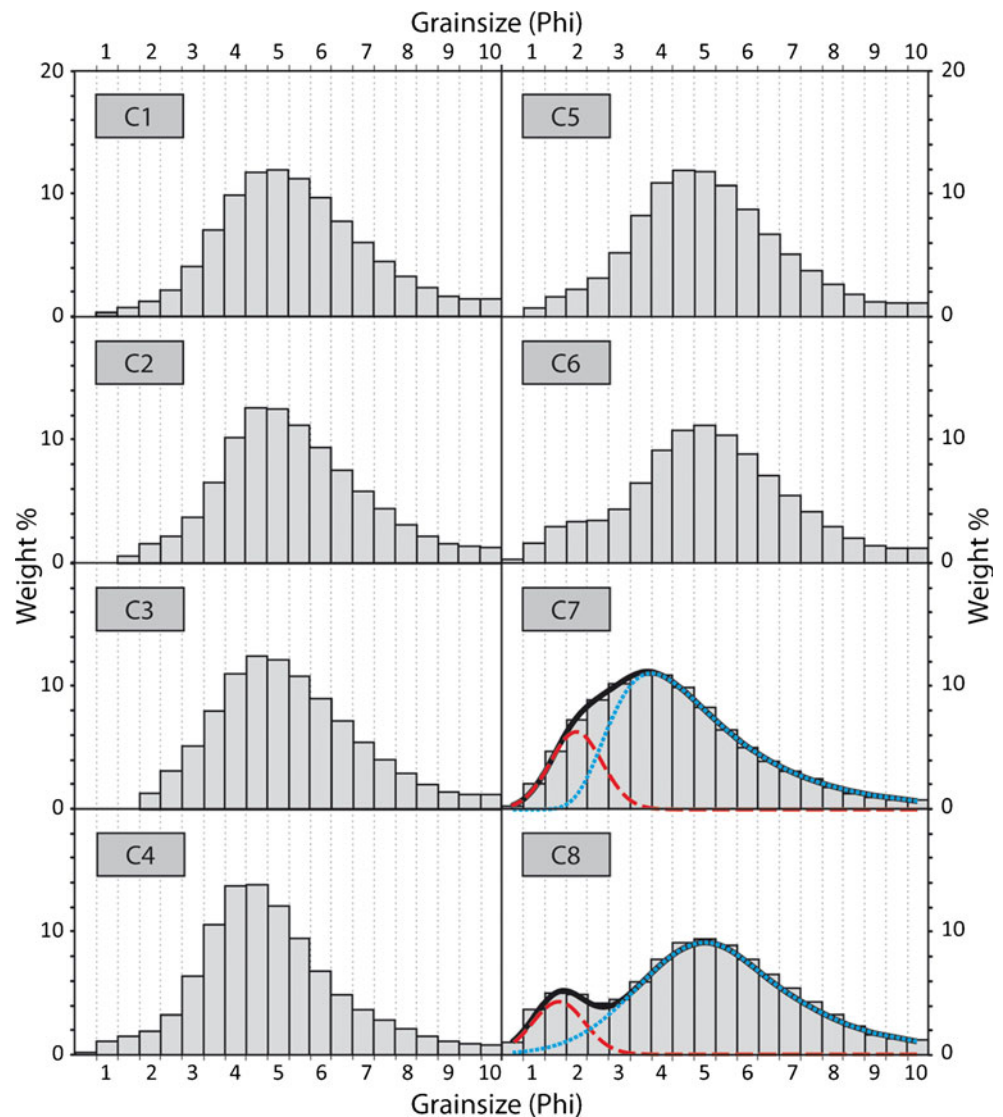


westward continuation of the area where the largest PF reached the Chambo River between Pillate village and Arrayan hill (Figs. 1c and 11). The area with x_{FS} above 20% is also coincident with downwind prolongation of PF deposits, which make a broad fan in the area located from the East of Cotalo village to Guilles Valley (Figs. 1c and 11). The map shows that x_{FS} varies from the most proximal to the distal locations parallel and perpendicular to an axis defined by the main flow direction of the PF (Fig. 11). These findings corroborate the idea that the fine subpopulations in our samples of the Quero plateau result from transport and deposition of ash particles previously elutriated from the PF on the volcano. As indicated by the grain-size distributions of Co-PF samples, particle sizes in Co-PF clouds are mostly above 4Φ and thus settle at a low Reynolds Number ($Re < 0.4$), which implies a low terminal velocity (Rose 1993; Bonadonna et al. 1998). These particles are thus easily transported several kilometres from the source prior to deposition. At Tungurahua, the emplacement of PF was restricted to nearby valleys (Puela, Chambo; Fig. 1c), but we infer that the Co-PF clouds were transported into the area of the main tephra plume dispersal, above the Arrayan relief and the Quero plateau, allowing fine ash sedimentation in the area. In contrast, fine ash particles in the main convective plume were transported far from the source and settled beyond the studied area. Observations of many Co-PF clouds in past eruptions indicate that Co-PF clouds rise to a lower elevation than that attained by vertical, jet-sustained volcanic columns. Such situations

are described e.g. for Reboubt in Alaska (Scott and McGimsey 1994), Mayon in the Philippines (Moore and Melson 1969) and Montserrat in the West Indies (Bonadonna et al. 2002). Satellite remote sensing data of the August 2006 Tungurahua eruption (Steffke et al. 2010) highlighted two plumes drifting at different elevations during the eruption, after the beginning of emplacement of the PF: the highest drifted between 17,500 and 24,000 m a.s.l. and the lower one between 7,250 and 10,500 m a.s.l. Given the low mobility of scoria flows and the relatively small volumes of their PF deposits, the Co-PF cloud was probably the lowest one. This configuration may explain why the fine ash from the Co-PF clouds settled on the Quero Plateau closer to the vent than the fine ash from the main column and plume, which were essentially transported beyond the studied area.

Figure 11 also suggests that the Co-PF cloud was locally influenced by confined atmospheric circulations, as evidenced by x_{FS} values increasing with distance from the PF depositional area in the secondary lobe contoured to the south-west by the red dotted line: distal samples located on the Igualata relief about 3,700 m a.s.l. show a large proportion of fine particles ($F_{15}=27\%$ and $F_{18}=25\%$), compared to proximal samples (12%, 14%, 19%) collected on the Plateau at about 3,400 m a.s.l., in the eastern continuation of the 600-m deep Igualata Valley. These grain-size distributions were classified into group C (Fig. 8) because they show poor sorting and a large coarse-grained subpopulation (Fig. 7 and see “Results”). We suggest that these local variations of grain-size distributions result from

Fig. 10 Grain-size distributions of the eight samples from the Co-PF deposit in weight %. Distributions C7 and C8 were deconvoluted in a minor coarse subpopulation (*dashed curve*) and a major fine subpopulation (*dotted curve*). *Thick solid curve* synthetic bimodal distribution resulting from the deconvolution procedure



the influence of topographic irregularities, and local winds running from the Guilles to the Iguatala valleys, on ash transport and deposition of the fine particles (Fig. 11). This process may have contributed to the irregularity of the isopach contours in the Iguatala area (Figs. 1c, 8, 11).

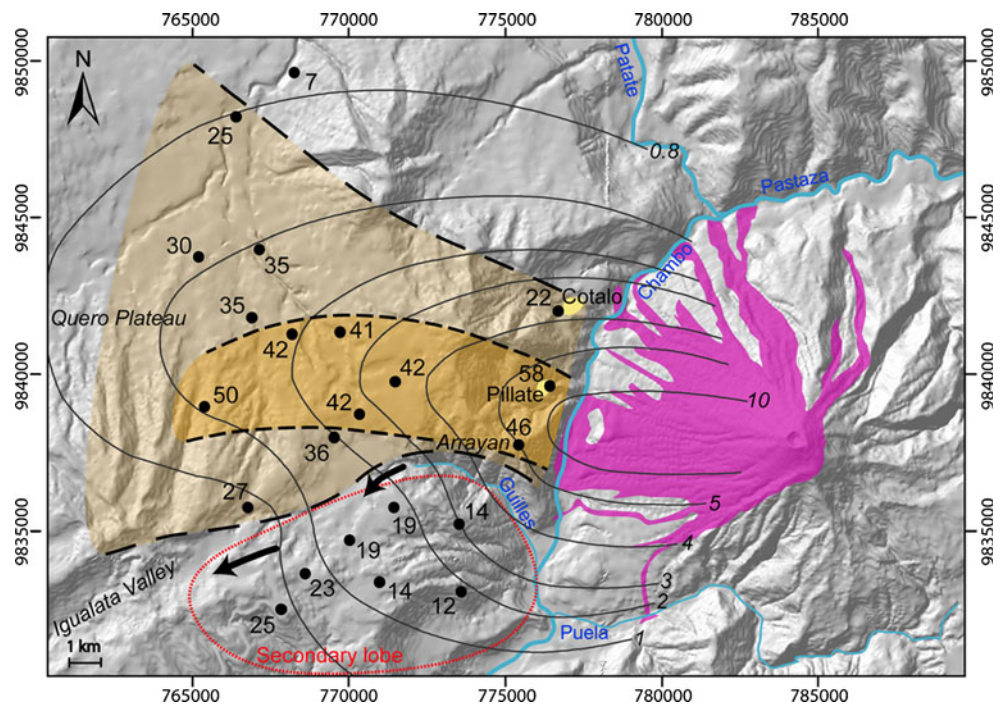
Depositional chronology of the stratigraphic units

Here, we propose a depositional chronology of the eruptive products based on witness accounts, stratigraphic evidence, grain-size results and interpretations presented in the previous sections. The plume was transported over the studied area from 2015 hours UTC on August 16 to about 1100 hours UTC on August 17 and consequently the emplacement of the tephra fall deposit from the main plume lasted for about 15 h, with a peak from 0100 to 0700 hours UTC on August 17. The emplacement of PF began around 2200 hours UTC on August 16 and continued as repeated pulses for about 5 to 6 h, as evidenced by seismic records

(Hall et al 2007), which led to multiple flow units in the deposits (see “Stratigraphy and sampling”). In the PF depositional area, the emplacement of the PF units occurred synchronously with the settling of the tephra fall particles from the main plume. Therefore, the tephra fall deposit locally occurs as thin coarse-grained scoria layers intercalated between PF units, or the PFall clasts were incorporated in the PF, with no depositional record as a distinct fallout layer. Hence, the PFall layers preserved on top of most PF deposits (chiefly on the western flanks) only reflect the final stage of the tephra fall event in the proximal area.

On the Quero plateau, i.e. west of the PF depositional area, the PFall layer consisted of a single bed composed of two grain-size subpopulations. Field observations indicated that the PFall layer occurred as a texturally sub-massive unit, i.e. with little or no lamination and stratification, and the fine-grained subpopulation occurred as a matrix between the scoria lapilli. For this reason, we infer that the main tephra plume and the Co-PF clouds reached the

Fig. 11 Weight fraction of the fine subpopulation (x_{FS}) in the bulk bimodal grain-size distributions of the PFall samples. *Solid dots* PFall sampling sites, *numerical labels* values for x_{FS} in weight %, *pink area* pyroclastic density current deposits, *light orange area bounded by long dashed lines* area where $40 > x_{FS} > 20\%$, *dark orange area bounded by short dashed lines* area where $x_{FS} > 40\%$. The *red dotted line* encloses the samples in the south-west lobe. *Solid arrows* local atmospheric currents, *solid curves* isopach contours in centimetres, *yellow area* inhabited areas mentioned in the text



Quero plateau at the same time, with synchronous deposition of the two grain subpopulations.

Consequences of synchronous deposition of Co-PF ash and tephra fall particles

The isopach map shows irregular, sub-bilobate contour lines in the area between Guilles and Iqualata valleys (Fig. 1c). Several processes may explain this deviation from the regular elliptical shape. Ernst et al. (1994) suggest that distinctive pressure distribution gradients may cause plume bifurcation, which in turn results in bilobate tephra thickness distributions. In the Tungurahua case, the plume height estimates (16–18 km above the vent) suggest a strong plume, but no evidence of strong cross wind was recorded. In addition, according to Ernst et al. (1994), bifurcated plumes show a region depleted in material between the two advancing lobes which should translate into sub-symmetrical tephra and grain-size distributions in the deposit. Such a pattern is not observed in our study: tephra fall thickness displays asymmetry and relief-dependent patterns, and grain-size distributions show no symmetrical arrangement in relation to the dispersal axis. Thus, the plume bifurcation process seems unlikely to explain the sub-bilobate shape of the isopach contours. A change in wind direction during plume drifting is another possible mechanism, but there are no wind records in the studied area to test that hypothesis. Yet, such wind shift effects have been observed frequently on longer timescales at Tungurahua, with notable influence on volcanic ash distribution (Le Pennec et al., personal communication),

and this process has been documented at other tropical volcanoes such as Cerro Negro, Nicaragua (Rose et al. 1973; Taylor 1969). However, as explained above, we interpret the lack of fine particles in the area contoured by the red dotted line in Fig. 11 as a result of local redistribution of the fine Co-PF ash, during fall deposition, by near-ground winds running from the Guilles to the Iqualata valleys, leading to low thickness values in this area (Fig. 1c). This redistribution suggests that the accumulation of the fine Co-PF particles had an impact on the final tephra thickness, particularly in the sampling localities where x_{FS} is above 20%, i.e. the area corresponding to the main depositional lobe (Fig. 11). The sub-bilobate shape of the thickness contour lines would thus be the result of a local “over-thickening” of the deposit due to the synchronous deposition of Co-PF ash and not from wind shift or bifurcation effects.

These interpretations raise the question of the impact of fine ash incorporation on volume calculations. We observed that the fine particles filled the void space between the lapilli grains of the PFall layer, which means that only a fraction of the fine particles contributes to the local “over-thickening” of the PFall layer. Thus, x_{FS} is not proportional to the PFall layer thickness but has a negligible effect on volume estimation.

Inference of eruptive type

The eruption type is determined here by referring to the classifications of Walker (1973) and Pyle (1989). Walker used two parameters, the dispersion index (D in square kilometres) and the fragmentation index (F in weight %). D

is the area enclosed in the isopach $1/100$ of the extrapolated thickness at the vent (T_0). Using the third exponential segment in the thinning rate (Fig. 4), we obtain $D=2,212 \text{ km}^2$. F is the weight percentage of ash finer than 1 mm in the deposit, at the site where the dispersal axis meets the $0.1 \times T_0$ isopach. F is estimated here using the grain-size distribution of sample F5, which closely matches the above requirements ($0.1 \times 37 \text{ cm} = 3.7 \text{ cm}$ isopach). Using the whole grain-size distribution, F is 71%, which locates the August 2006 eruption in the vulcanian field of Walker's classification diagram (Fig. 12). However, the phenomenology of the activity and the lithology of the deposits do not support a vulcanian eruption type: the tephra layer is essentially composed of juvenile, highly vesicular scoria clasts ($\sim 95\%$) and the eruptive column was sustained over 6 h. In addition, the 8-month-long activity preceding the August 2006 event (see “Geological setting and recent volcanic activity”) indicates persistent degassing from an open conduit system, which is unlike the vulcanian

behaviour documented at other volcanoes (Stix et al. 1997; Morrissey and Mastin 2000). Walker's classification relies on tephra fall deposits and does not account for the possible mixing of grain populations from different origins, as is the case in the PFall layer. Data processing and deconvolution have allowed us to isolate the coarse-grained plume-derived subpopulation of the PFall layer and allowed us to recalculate the F index for the F5 sample using only the distribution of the coarse subpopulation and obtained 47%, which places the 2006 Tungurahua eruption in the plinian field (Fig. 12).

Pyle's classification is based on the calculation of parameters b_c , the maximum clast half-distance and b_t , the thickness half-distance (Pyle 1989). We obtained a b_c of 3.1 km and a b_t of 1.2 km (Figs. 4 and 5). As a result, the data plots near the limit between plinian and subplinian fields (Fig. 12). Pyle's classification relies on maximum clast size, which corresponds to the coarsest fraction of our samples. Hence, when the fine Co-PF-derived subpopulation is removed from the analysis, the August 2006 eruption is described as plinian in both Walker and Pyle classifications of eruptive types. Based upon the dispersal model of Carey and Sparks (1986), Pyle's classification states that plinian eruptions have total column heights $>29 \text{ km}$ above the depositional area ($\sim 3 \text{ km}$ a.s.l. in the case of Tungurahua Volcano). Although the August 2006 event plots in the plinian field, our data and observations do not fully support this minimal column height. Our maximum clast size data yield a height between 16 and 18 km above the vent, which is significantly lower than the limit proposed in Pyle's definition of plinian eruptive type. Satellite-based data suggest a column height of 24 km a.s.l. (Steffke et al. 2010), which is still 8 km below the plinian minimum of Pyle's classification.

Our ground-based evaluation of the eruption size supports a VEI 3, which corresponds to a “moderate-large” event with column height of 3–15 km in the original VEI Table of Newhall and Self (1982). The steep-sloped proximal thinning rate (Fig. 4) contrasts with those of most widespread sheet-like deposits of typical Plinian eruptions (Houghton et al. 2000) and is more akin to that of many violent strombolian to subplinian eruptions (e.g. Arrighi et al. 2001; Pioli et al. 2008). In addition, componentry analyses, scoria clast textures (to be presented elsewhere) and block-rich, small-volume scoria flow deposits, all point to a subplinian, rather than a plinian eruption type.

The findings obtained at Tungurahua suggest that the limit between subplinian (typically VEI 3) and plinian (typically VEI 4–5) fields should be placed at a higher dispersal limit in Walker's and Pyle's classification schemes and that an improved determination of the eruptive style should include componentry and textural data.

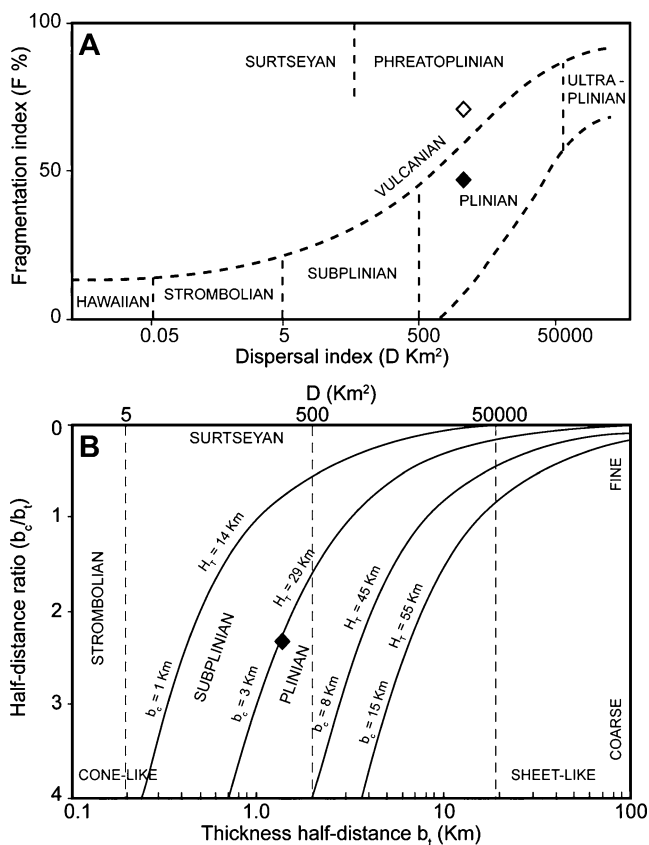


Fig. 12 **a** Classification scheme of eruption types after Walker (1973). *Open diamond* classification of the August 16–17, 2006 eruption of Tungurahua using the bulk grain-size distribution of the sample F5 for the calculation of F . *Solid diamond* classification using the fine subpopulation of the grain-size distribution of the sample F5 for the calculation of F . **b** Classification scheme of the eruptive types after Pyle (1989). *Solid diamond* classification of the August 16–17, 2006 eruption of Tungurahua

Conclusion

The August 16–17, 2006 Tungurahua eruption in Ecuador witnessed the emplacement of numerous scoria flows and the deposition of a widespread tephra layer west of the volcano. We investigated the distribution, thinning rate and volume of the tephra to determine the size of the eruption. A bulk tephra volume in the range $47\text{--}67 \times 10^6 \text{ m}^3$ supports a VEI 3 event, consistent with a calculated column height of 16–18 km above the vent, i.e. smaller than the VEI 4 inferred from remote sensing data of Steffke et al. (2010). This has been the most common eruption size at Tungurahua since 3 ka (Le Pennec et al. 2006, 2008).

Sieve and laser diffraction analyses of our pyroclastic fall layer samples reveal bimodal grain-size distributions. We developed an algorithm which allows us to identify two grain-size subpopulations in the deposit with distinct characteristics, thus revealing different transport-depositional processes. The coarse-grained subpopulation is interpreted as the result of transportation and sedimentation from the main volcanic plume, which drifted west from the vertical tephra column. The positively skewed fine-grained subpopulation is unevenly distributed laterally in the pyroclastic fall layer and shares grain-size similarities with the elutriated co-pyroclastic flow ash cloud deposits preserved on top of the scoria flow deposits. We show that the high fine particle content in the fall layer coincides with the downwind prolongation of the pyroclastic flow deposits. These results indicate that bimodal grain-size distribution in fallout layer results from synchronous deposition of lapilli from the main plume and fine ash elutriated from scoria flows. We found no evidence for ash aggregation or plume bifurcation processes to explain these bimodal grain-size distributions.

Our study indicates that synchronous deposition of coarse-grained lapilli from a volcanic plume with fine-grained ash during concomitant emplacement of pyroclastic density currents is an additional mechanism to explain bimodal grain-size distributions in tephra fall layers. Moreover, our work shows that inappropriate grain-size data processing may result in inadequate eruptive type characterization. Tephra dispersal characteristics of the violent August 2006 Tungurahua eruption place it in the plinian field of current classification schemes, but our investigation favours a subplinian eruption type.

Acknowledgements This work is part of a PhD project by JE and has been completed in the context of a French-Ecuadorian cooperation program. Discussions with P Ramon, P Samaniego, H Yepes, C Robin, K Kelfoun, P Hall, P Mothes and many other individuals in the Tungurahua region improved our understanding of the August 2006 event. Reviews of the manuscript by RJ Carey and D Andronico and editorial handling by R Cioni and J White are warmly acknowledged.

Appendix

Particle size distributions (PSD) of natural deposits commonly show polymodal and asymmetric distributions usually interpreted as a combination of various physical processes that cannot be described by a single log-normal distribution. The aim of LOGN_2D algorithm (LOGNormal Distribution Deconvolution) is to decipher natural composite PSD by a sum of independent PSDs accounting for distinct processes. This fully automated algorithm is based on a discretized Weibull-type distribution whose flexibility permits easy interpolation between a wide range of distributions and positive skewness modelling.

The Weibull distribution is defined through a probability density function of particles with diameter (x) using the two parameters (k) and (λ):

$$f_w(x; k, \lambda) = \left(\frac{k}{\lambda}\right) \left(\frac{x}{\lambda}\right)^{(k-1)} \exp\left(-\frac{x}{\lambda}\right)^k \quad \text{for } x > 0 \quad (\text{A1})$$

The shape factor (k) permits to model from exponential ($k=1$) to Gaussian ($k=3$) shapes, hence allowing non log-normal distribution modelling. The shift factor (λ) depends on the mode (μ) and is defined by:

$$\lambda = \mu \left(\frac{k-1}{k}\right)^{-\frac{1}{k}} \quad (\text{A2})$$

The cumulative distribution function for the Weibull distribution is:

$$F(x; k, \lambda) = 1 - \exp\left(-\frac{x}{\lambda}\right)^k \quad \text{for } x \geq 0 \quad (\text{A3})$$

Then, the Weibull distribution can be used to generate a combination of several components in order to model a natural composite distribution as:

$$f(x)_{\text{comp}} = w_1 f_1(x) + w_2 f_2(x) + \dots + w_n f_n(x) \quad (\text{A4})$$

and

$$F(x)_{\text{comp}} = w_1 F_1(x) + w_2 F_2(x) + \dots + w_n F_n(x) \quad (\text{A5})$$

where w_i is the weight of each component that represents their relative fraction following:

$$\sum_{i=1}^n w_i = 1 \quad (\text{A6})$$

The deconvolution of the natural distribution can be achieved by best-fit matching of synthetic and natural data. The inversion procedure uses a least-square estimation method based on the minimization function $S(x)$ between the natural and the synthetic distribution.

$$S(x) = \sum \left[f(x)_{\text{nat}} - f(x)_{\text{synth}} \right]^2 \quad (\text{A7})$$

Variable parameters (k, λ, μ and w) are optimized during iterative calculations until the fitness criterion between synthetic and natural distributions is reached.

The accuracy of the deconvolution procedure is controlled for the whole sample population verifying the similarity between the Inman's parameters ($Md_{\Phi}, \sigma_{\Phi}, Sk$) for the natural bulk distribution, and the Inman's parameters for the synthetic bimodal distribution (Fig. 13). The data points are distributed on a line with the equation $y=x$, which suggests that the deconvolution gave realistic results.

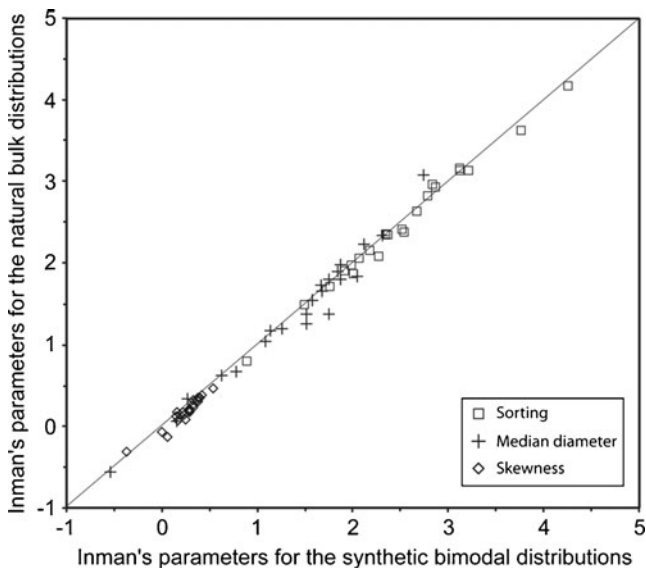


Fig. 13 Deconvolution checking-graph: correlation between the Inman's parameters calculated for the natural bulk distributions and the Inman's parameters calculated for the synthetic bimodal distributions of the whole 22 Pfall samples

References

- Arana-Salinas L, Siebe C, Macías JL (2010) Dynamics of the ca. 4965 yr 14 C BP "Ochre Pumice" Plinian eruption of Popocatepetl volcano, México. *J Volcanol Geotherm Res* 192:212–231
- Arellano S, Hall M, Samaniego P, Le Pennec J-L, Ruiz A, Molina I, Yepes H (2008) Degassing patterns of Tungurahua volcano (Ecuador) during the 1999–2006 eruptive period, inferred from remote spectroscopic measurements of SO₂ emissions. *J Volcanol Geotherm Res* 176:151–162
- Arrighi S, Principe C, Rosi M (2001) Violent strombolian and subplinian eruptions at Vesuvius during post-1631 activity. *Bull Volcanol* 63:126–150
- Barberi F, Coltelli M, Ferrara G, Innocenti F, Navarro JM, Santacrose R (1988) Plio-Quaternary volcanism in Ecuador. *Geol Mag* 125:1–14
- Biaass S, Bonadonna C (2010) A quantitative uncertainty assessment of eruptive parameters derived from tephra deposits: the example of two large eruptions of Cotopaxi volcano, Ecuador. *Bull Volcanol* 73:73–90
- Bonadonna C, Ernst GGJ, Sparks RSJ (1998) Thickness variations and volume estimates of tephra fall deposits: the importance of particle Reynolds number. *J Volcanol Geotherm Res* 81:173–187
- Bonadonna C, Mayberry GC, Calder ES, Sparks RSJ, Choux C, Jackson P, Lejeune AM, Loughlin SC, Norton GE, Rose WI, Ryan G, Young SR (2002) Tephra fallout in the eruption of Soufriere Hills Volcano, Montserrat. In: Druitt TH, Kokelaar BP (eds) *The eruption of Soufrière Hills Volcano, Montserrat, from 1995 to 1999*. Geological Society, London, pp 483–516, 21
- Bonadonna C, Houghton BF (2005) Total grain-size distribution and volume of tephra-fall deposits. *Bull Volcanol* 67:441–456
- Brazier S, Sparks RSJ, Carey SN, Sigurdsson H, Westgate JA (1983) Bimodal grain size distribution and secondary thickening in air-fall ash layers. *Nature* 301:115–119
- Carey RJ, Houghton BF, Thordarson T (2009) Tephra dispersal and eruption dynamics of wet and dry phases of the 1875 eruption of Askja Volcano, Iceland. *Bull Volcanol* 72:259–278
- Carey RJ, Houghton BF (2010) "Inheritance": An influence on the particle size of pyroclastic deposits. *Geology* 38:347–350
- Carey S, Sparks RSJ (1986) Quantitative models of the fallout and dispersal of tephra from volcanic eruption columns. *Bull Volcanol* 48:109–125
- Costantini L, Bonadonna C, Houghton B, Wehrmann H (2009) New physical characterization of the Fontana Lapilli basaltic Plinian eruption, Nicaragua. *Bull Volcanol* 71:337–355
- Darteville S, Ernst GGJ, Stix J, Bernard A (2002) Origin of the Mount Pinatubo climatic eruption cloud: Implications for volcanic hazards and atmospheric impacts. *Geology* 30:663–666
- Ernst GGJ, Davis JP, Sparks RSJ (1994) Bifurcation of volcanic plumes in a crosswind. *Bull Volcanol* 56:159–169
- Evans JR, Huntoon JE, Rose WI, Varley NR, Stevenson JA (2009) Particle sizes of andesitic ash fallout from vertical eruptions and co-pyroclastic flow clouds, Volcan de Colima, Mexico. *Geology* 37:935–938
- Fee D, Garces M, Steffke A (2010) Infrasound from Tungurahua Volcano 2006–2008: Strombolian to Plinian eruptive activity. *J Volcanol Geotherm Res* 193:67–81
- Fisher R (1964) Maximum Size, Median Diameter, and Sorting of Tephra. *J Geophys Res* 69:341–355
- Fierstein J, Nathenson M (1992) Another look at the calculation of fallout tephra volumes. *Bull Volcanol* 54:156–167
- Fierstein J, Houghton BF, Wilson CJN, Hildreth W (1997) Complexities of plinian fall deposition at vent: an example from the 1912 Novarupta eruption (Alaska). *J Volcanol Geotherm Res* 76:215–227
- Freundt A, Schmincke H (1992) Abrasion in pyroclastic flows. *Geol Rundsch* 81:383–389
- Freundt A, Wilson CJN, Carey SN (2000) Ignimbrites and block-and-ash flow deposits. In: Sigurdsson H (ed) *Encyclopedia of Volcanoes*. Academic Press, New York, pp 581–599
- Gouhier M, Donnadieu F (2008) Mass estimations of ejecta from Strombolian explosions by inversion of Doppler radar measurements. *J Geophys Res* 113:B10202
- Hall M, Robin C, Beate B, Mothes P, Monzier M (1999) Tungurahua Volcano, Ecuador: structure, eruptive history and hazards. *J Volcanol Geotherm Res* 91:1–21
- Hall M, Mothes P, Ramon P, Arellano S, Barba D, Palacios P (2007) Dense pyroclastic flows of the 16–17 august 2006 Eruption of Tungurahua Volcano, Ecuador. AGU Joint Assembly, Acapulco, Mexico
- Houghton BF, Wilson CJN, Pyle DM (2000) Pyroclastic Fall Deposits. In: Sigurdsson H (ed) *Encyclopedia of Volcanoes*. Academic Press, New York, pp 555–570
- Houghton BF, Wilson CJN, Fierstein J, Hildreth W (2004) Complex proximal deposition during the Plinian eruptions of 1912 at Novarupta, Alaska. *Bull Volcanol* 66:95–133
- Inman DL (1952) Measures for describing the size distribution of sediments. *J Sediment Res* 22:125–145

- Kelfoun K, Samaniego P, Palacios P, Barba D (2009) Testing the suitability of frictional behaviour for pyroclastic flow simulation by comparison with a well-constrained eruption at Tungurahua volcano (Ecuador). *Bull Volcanol* 71:1057–1075
- Le Pennec J-L, Hall ML, Robin C, Bartomioli E (2006) Tungurahua volcano - Late Holocene activity. Field Guide A1. IAVCEI (Editor), Fourth International Conference "Cities on Volcanoes", Quito, Ecuador
- Le Pennec J-L, Jaya D, Samaniego P, Ramón P, Moreno Yáñez S, Egred J, Van der Plicht J (2008) The AD 1300–1700 eruptive periods at Tungurahua volcano, Ecuador, revealed by historical narratives, stratigraphy and radiocarbon dating. *J Volcanol Geotherm Res* 176:70–81
- Molina I, Kumagai H, Le Pennec J-L, Hall M (2005) Three-dimensional P-wave velocity structure of Tungurahua Volcano, Ecuador. *J Volcanol Geotherm Res* 147:144–156
- Moore JG, Melson WG (1969) Nuées Ardentes of the 1968 Eruption of Mayon Volcano, Philippines. *Bull Volcanol* 33:600–620
- Morrissey MM, Mastin LG (2000) Vulcanian eruptions. In: Sigurdsson H (ed) *Encyclopedia of Volcanoes*. Academic Press, New York, pp 463–475
- Newhall CG, Self S (1982) Volcanic Explosivity Index (VEI): An estimate of explosive magnitude for historical volcanism. *J Geophys Res* 87:1231–1238
- Pioli L, Erlund E, Johnson E, Cashman K, Wallace P, Rosi M, Granados HD (2008) Explosive dynamics of violent Strombolian eruptions: The eruption of Parícutin Volcano 1943–1952 (Mexico). *Earth Planet Sci Lett* 271:359–368
- Pyle DM (1989) The thickness, volume and grain-size of tephra fall deposits. *Bull Volcanol* 51:1–15
- Rose WI, Bonis S, Stoiber R, Keller M, Bickford T (1973) Studies of volcanic ash from two recent Central American eruptions. *Bull Volcanol* 37:338–364
- Rose WI (1993) Comment on 'another look at the calculation of fallout tephra volumes' by Judy Fierstein and Manuel Nathenson. *Bull Volcanol* 55:372–374
- Rose WI, Self S, Murrow P, Bonadonna C, Durant A, Ernst GGJ (2008) Nature and significance of small volume fall deposits at composite volcanoes: Insights from the October 14, 1974 Fuego eruption, Guatemala. *Bull Volcanol* 70:1043–1067
- Rose WI, Durant AJ (2009) Fine ash content of explosive eruptions. *J Volcanol Geotherm Res* 186:32–39
- Samaniego P, Le Pennec J-L, Robin C, Hidalgo S (2011) Petrological analysis of the pre-eruptive magmatic process prior to the 2006 explosive eruptions at Tungurahua. *J Volcanol Geotherm Res* 199:69–84
- Scott WE, McGimsey RG (1994) Character, mass, distribution, and origin of tephra-fall deposits of the 1989–1990 eruption of redoubt volcano, south-central Alaska. *J Volcanol Geotherm Res* 62:251–272
- Sparks RSJ, Self S, Walker GPL (1973) Products of Ignimbrite Eruptions. *Geology* 1:115–118
- Steffke AM, Fee D, Garces M, Harris A (2010) Eruption chronologies, plume heights and eruption styles at Tungurahua Volcano: Integrating remote sensing techniques and infrasound. *J Volcanol Geotherm Res* 193:143–160
- Stix J, Torres R, Narváez M, Cortés G, Raigosa J, Gómez D, Castonguay R (1997) A model of vulcanian eruptions at Galeras volcano, Colombia. *J Volcanol Geotherm Res* 77:285–303
- Sulpizio R (2005) Three empirical methods for the calculation of distal volume of tephra-fall deposits. *J Volcanol Geotherm Res* 145:315–336
- Taylor PS (1969) Soluble material on volcanic ash. Unpublished MA Thesis, Dartmouth College, Hanover, N. H
- Walker GPL (1971) Grain-size characteristics of pyroclastic deposits. *J Geol* 79:696–714
- Walker GPL (1973) Explosive volcanic eruptions — a new classification scheme. *Geol Rundsch* 62:431–446
- Walker GPL (1981a) Characteristics of two phreatoplinian ashes, and their water-flushed origin. *J Volcanol Geotherm Res* 9:395–407
- Walker GPL (1981b) Generation and dispersal of fine ash and dust by volcanic eruptions. *J Volcanol Geotherm Res* 11:81–92
- Watt SFL, Pyle DM, Mather TA, Martin RS, Matthews NE (2009) Fallout and distribution of volcanic ash over Argentina following the May 2008 explosive eruption of Chaitén, Chile. *J Geophys Res* 114:B04207
- Wohletz KH, Sheridan MF, Brown WK (1989) Particle size distributions and the sequential fragmentation/transport theory applied to volcanic ash. *J Geophys Res* 94:15703–15721